

Pulsar radio emission mechanism – II. On the origin of relativistic Langmuir solitons in pulsar plasma

Sk. Minhajur Rahaman ¹★, Dipanjan Mitra ^{1,2}, George I. Melikidze^{2,3} and Taras Lakoba⁴

¹National Centre for Radio Astrophysics, Tata Institute of Fundamental Research, Post Bag 3, Ganeshkind, Pune 411007, India

²Janusz Gil Institute of Astronomy, University of Zielona Góra, ul Szafrana 2, PL-65-516 Zielana Góra, Poland

³Abastumani Astrophysical Observatory, Ilia State University, 3–5 Cholokashvili Ave., Tbilisi 0160, Georgia

⁴Department of Mathematics and Statistics, University of Vermont, Burlington, VT 05401, USA

Accepted 2022 August 8. Received 2022 July 14; in original form 2022 April 24

ABSTRACT

Observations suggest that coherent radio emission from pulsars is excited in a dense pulsar plasma by curvature radiation from charge bunches. Numerous studies propose that these charge bunches are relativistic charge solitons that are solutions of the non-linear Schrödinger equation (NLSE) with a group velocity dispersion (G), cubic non-linearity (q), and non-linear Landau damping (s). The formation of stable solitons crucially depends on the parameters G , q , and s as well as the particle distribution function (DF). In this work, we use realistic pulsar plasma parameters obtained from observational constraints to explore the parameter space of NLSE for two representative DFs of particles' momenta: Lorentzian (long-tailed) and Gaussian (short-tailed). The choice of DFs critically affects the value of $|s/q|$, which, in turn, determines whether solitons can form. Numerical simulations show that well-formed solitons are obtained only for small values of $|s/q| \lesssim 0.1$, while for moderate and higher values of $|s/q| \gtrsim 0.5$ soliton formation is suppressed. Small values for $|s/q| \sim 0.1$ are readily obtained for long-tailed DF for a wide range of plasma temperatures. On the other hand, short-tailed DF provides these values only for some narrow range of plasma parameters. Thus, the presence of a prominent high-energy tail in the particle DF favours soliton formation for a wide range of plasma parameters. Besides pair plasma, we also include an iron ion component and find that they make a negligible contribution in either modifying the NLSE coefficients or contributing to charge separation.

Key words: plasmas – radiation mechanisms: non-thermal – relativistic processes – waves – pulsars: general.

1 INTRODUCTION

Understanding the mechanisms of coherent radio emission from pulsars has been a challenging astrophysical problem since the discovery of pulsars. Most models of coherent radio emission involve growth of instability in strongly magnetized relativistically streaming pair plasma and are broadly classified into maser or antenna mechanisms (see e.g. Ginzburg, Zheleznyakov & Zaitsev 1969; Kazbegi, Machabeli & Melikidze 1991; Melrose 1995). Recent single-pulse polarization observations, however, strongly favour the antenna mechanism, where the radio emission is excited in pair plasma by coherent curvature radiation (hereafter CCR) due to motion of charge bunches along curved magnetic field lines (Mitra, Gil & Melikidze 2009).

Observations have further established that the radio emission detaches the pulsar magnetosphere from around 500 km above the neutron star surface (Kijak & Gil 1997, 1998; Mitra 2017), where the magnetic field topology is purely dipolar (Mitra & Li 2004). At the radio emission region, due to enormously strong magnetic field, the motion of plasma particles can be approximated to be one-dimensional. The primary source of pair plasma in pulsars is magnetic pair production by high-energy photons at the polar cap. In our study, we consider the scenario for $\mathbf{\Omega} \cdot \mathbf{B} < 0$ in which a charge-

starved inner accelerating region (IAR) region develops above the polar cap where unscreened electric field exists and the primary pairs are formed and accelerated to extremely high Lorentz factors γ_p (see Sturrock 1971; Ruderman & Sutherland 1975, hereafter RS75). One kind of charges is accelerated away from the polar cap, and these charges can radiate high-energy photons, which in turn produce a cascade of secondary pair plasma moving with Lorentz factor γ_s . Several lines of evidence suggest a strongly non-dipolar magnetic field topology at the surface (Geppert 2017; Arumugasamy & Mitra 2019; Mitra et al. 2020) and in such strong fields copious pair creation can occur. As a result, dense and hot pair plasma is produced. The density of the pair plasma exceeds the co-rotation Goldreich–Julian charge density (Goldreich & Julian 1969) by a factor $\kappa \sim 10^4$ – 10^5 (Arendt & Eilek 2002), streaming with a bulk Lorentz factor $\gamma_s \approx 10^2$ – 10^3 in the observer's frame of reference. Observations of pulsar wind nebulae have also confirmed the presence of a dense pair plasma (Blasi & Amato 2011). In the IAR, the charge that accelerates towards the polar cap can heat the polar cap to high temperatures, and X-ray observations have revealed the presence of such hot polar cap in several pulsars. However, extremely high temperatures could be expected if the polar cap discharges were to occur under pure vacuum conditions, which is not observed. Hence, to properly account for the polar cap temperature, Gil, Melikidze & Geppert (2003) suggested that the IAR is a partially screened gap (PSG). The PSG model is a variant of the pure vacuum models and takes into consideration the binding energy of iron ions on the surface. The

* E-mail: rahaman.minhajur93@gmail.com

heating due to backflowing charges unpins iron ions from the surface and contributes close to 90 per cent of the co-rotational charge density. The flow of ions is thermostatically regulated as follows: if the surface is heated beyond some critical temperature T_{ion} , the gap closes completely, while for surface temperature below T_{ion} the gap is partially screened. Under equilibrium conditions, the surface temperature is only slightly offset from the critical temperature and any greater offset is corrected on time-scales of a few hundred nanoseconds. Owing to a heavier mass, the iron ions are accelerated to Lorentz factors, γ_{ion} , close to the Lorentz factor of the secondary plasma, γ_s . The PSG model is a very successful phenomenological model for explaining the subpulse drift rates, mode changing, and thermal X-ray luminosity (see e.g. Szary, Melikidze & Gil 2015; Basu et al. 2016; Rahaman et al. 2021). The presence of an additional iron component in the pulsar plasma is hence an important ingredient. To summarize, magnetically induced pair cascades and outflow of ions above the polar cap give rise to an ultrarelativistic, collisionless, and multicomponent plasma outflow strictly along the open magnetic field lines of the pulsar (Goldreich & Julian 1969; Sturrock 1971; RS75).

On the theoretical front, the formation of stable charge bunches capable of explaining coherent radio emission from pulsars has been a long-standing puzzle (Ginzburg et al. 1969; Melrose & Gedalin 1999). Earlier studies suggested that in the radio emission zone linear Langmuir waves can be unstable due to plasma two-stream instability, and as a result, linear charge bunches can radiate coherently (RS75; Cheng & Ruderman 1977). However, it was soon realized that the very high-frequency linear Langmuir waves disperse the linear bunch well before it can emit coherently (Lominadze et al. 1986; Melrose & Gedalin 1999; Melikidze, Gil & Pataraya 2000, hereafter MGP00; Lakoba, Mitra & Melikidze 2018). In order to circumvent this problem, studies like those of Karpman et al. (1975), Melikidze & Pataraya (1980), Pataraya & Melikidze (1980), Melikidze & Pataraya (1984), and MGP00 explored the non-linear regime of Langmuir waves to provide a time-stable charge distribution. A necessary condition for exploring the non-linear regime is the presence of strong plasma turbulence in the linear regime, and Asseo & Melikidze (1998) and more recently Rahaman, Mitra & Melikidze (2020, hereafter Paper I) showed that very effective two-stream instabilities can provide this condition within 1000 km from the neutron star surface. Recent particle-in-cell simulations by Manthei et al. (2021) also established the presence of strong Langmuir turbulence in pulsar plasma. In the non-linear regime, the linear Langmuir waves with frequency ω_1 interact to produce low-frequency beats ($\Delta\omega \ll \omega_1$) that modulate the envelope E of the high-frequency linear Langmuir waves. The linear waves do not maintain a definite phase relationship with each other over the spatial scale. As a result, the envelope electric field E itself has a white-noise character and the initial envelope electric field is assumed to be completely disordered. The envelope E is governed by the non-linear Schrödinger equation (hereafter NLSE) with a non-local term (see e.g. Melikidze & Pataraya 1980; Pataraya & Melikidze 1980; Melikidze & Pataraya 1984; Melikidze et al. 2000):

$$i\partial_t E + G\partial_{xx}^2 E + q|E|^2 E + s\mathcal{P} \int dx' V(x, x') = 0. \quad (1)$$

The term $G\partial_{xx}^2 E$ represents the group velocity dispersion (hereafter GVD) of the linear Langmuir waves. The term $q|E|^2 E$ represents cubic non-linearity (hereafter CNL). The non-local term $s\mathcal{P} \int dx' V(x, x')$ represents the non-linear Landau damping (hereafter NLD). NLD represents a resonant interaction at the group velocity of the Langmuir waves with plasma particles. The interaction

at group velocity not only gives rise to NLD but also modifies CNL. The coefficient q represents the strength of local (in space) non-linear interactions. The coefficient s represents a non-local interaction via a cascade of energy from higher length-scales (lower wave numbers) to shorter length-scales (higher wave numbers; see Section 3.3). The time-stable solution of equation (1) is referred to as solitons, which are considered as candidates for charge bunches giving rise to CCR at radio wavelengths.

In the absence of NLD, equation (1) represents a purely local NLSE. Lighthill (1967) showed that this equation admits analytical solutions as solitons, provided that the so-called Lighthill condition represented as

$$Gq > 0 \quad (2)$$

is satisfied and the initial electric wave field is a phase-coherent plane wave. Previous studies by Melikidze & Pataraya (1978, 1980), Pataraya & Melikidze (1980), Melikidze & Pataraya (1984), and MGP00 neglected NLD to get analytical solutions and conjectured that the Lighthill condition can be satisfied in pulsar pair plasma. Lakoba et al. (2018, hereafter LMM18) pursued numerical solution of equation (1) and confirmed a previously known fact that purely cubic NLSE cannot give rise to long-living solitons either from an initially disordered electric field E (the most natural state for the Langmuir envelope) or even from a phase-coherent plane wave-like initial electric field. More importantly, LMM18 found that for finite but sufficiently weak non-locality of the non-linear interactions, i.e. for finite but small values of $|s/q|$, formation of long-living solitons did occur. LMM18 estimated a range of $|s/q|$ values where such formation takes place, but did not address the question whether that range values of $|s/q|$ could actually exist under generic hot plasma conditions in pulsar magnetosphere. Answering it requires modelling of group velocity interaction of Langmuir waves with plasma particles, which depends on the choice of particle momentum distribution function (hereafter DF). Therefore, for such modelling, one needs to consider physically motivated and representative forms of DF in pulsar plasma. To our knowledge, this has not been done in any previous studies and thus has been an open issue.

In order to obtain solitons that can have properties of a charge bunch, the electron–positron DFs of the pair plasma must separate to create charge-separated structures in the configuration space. These charge-separated structures have been proposed as candidates for CCR charge bunches. MGP00 also suggested that the presence of heavier ion species, that had been proposed by the PSG model, can also aid in charge separation. However, the relative contribution of the two effects has not been studied before. Thus, the presence of ions is an important ingredient that has not been considered in earlier studies and hence also needs to be explored.

This study is focused on addressing the two open issues stated above. Namely, it has the following objectives. First, we want to estimate the ratio of s/q and explore the parameter space for pulsar plasma DFs and then simulate numerically the soliton profiles for the s/q range obtained. Secondly, we want to estimate the relative contribution of the separation of the electron–positron DF and the presence of ions in determining the charge separation in soliton profiles.

The paper is organized as follows. We introduce the NLSE in Section 2. The parameter space and soliton solutions of NLSE are explored in Section 3. Typical estimates of the charge separation of the Langmuir solitons are presented in Section 4. Our conclusions are summarized in Section 5.

2 INTRODUCTION TO NLSE WITH NLD

We identify three frames of reference. We have a plasma frame of reference (hereafter PFR) where the average velocity of the pair plasma particles is zero. The PFR moves with a Lorentz factor γ_s with respect to the observer frame of reference (OFR). The moving frame of reference (MFR) moves with respect to PFR at the group velocity of the linear Langmuir waves v_{gr} in PFR. Quantities in MFR are primed while the quantities in PFR are unprimed. The envelope (E) of the Langmuir waves is governed by the NLSE with the NLD,

$$i \frac{\partial E}{\partial \tau'} + G \frac{\partial^2 E}{\partial \xi'^2} + q E |E|^2 + s \frac{1}{\pi} \mathcal{P} \int_{-\infty}^{+\infty} d\xi'' \frac{|E(\xi'', \tau')|^2}{\xi' - \xi''} E = 0, \quad (3)$$

where the quantities τ' and ξ' represent the slow time and space variables in MFR, respectively (see equation A1 and A2 in Appendix A; the appendices are available online). It must be noted that while the equation itself is written in MFR, the coefficients (G , q , s) are computed in PFR. Here, the symbol \mathcal{P} stands for the principal value Cauchy integral.

A complete formal derivation of equation (3) is found in Appendix A. Equation (3) was derived by MGP00 (see also Melikidze & Pataraya 1980; Pataraya & Melikidze 1980; Melikidze & Pataraya 1984), however, our derivation differs from MGP00 in one crucial aspect. It allows contributions for arbitrary species of mass m_α and charge e_α (in particular, ions) to be taken into account, while the original derivation of MGP00 was for an electron–positron plasma. Inclusion of ions as an additional plasma component and evaluation of their contribution to the coefficients of the NLSE (3) is one of the stated goals of this study. It must also be noted that in our derivation, certain integrals where MGP00 missed the charge dependences, have been updated. The setup for the introduction of ions and tracking the charge dependence of multiple species is described in Appendix B.

2.1 The NLSE coefficients

The coefficients of equation (3) can be represented in their dimensionless form as (see MGP00; also equations B6, B8, and B11 of Appendix B)

$$G = \frac{c^2}{\omega_p} \left(\gamma_{gr}^3 g_d \right) = \frac{c^2}{\omega_p} G_d, \quad (4)$$

$$q = \frac{1}{\omega_p} \left(\frac{e}{m_e c} \right)^2 q_d, \quad (5)$$

$$s = \frac{1}{\omega_p} \left(\frac{e}{m_e c} \right)^2 s_d, \quad (6)$$

where the coefficients (G_d , q_d , s_d) are dimensionless. We will first present an estimate for the plasma frequency ω_p in equations (4)–(6) and then discuss factors that affect (G_d , q_d , s_d). Values of these coefficients themselves are discussed later in the text.

The typical plasma frequency at a distance r from the neutron star surface in OFR is

$$\omega_{p,\text{OFR}} = \sqrt{\frac{4\pi n_s e^2}{m_e}}, \quad (7)$$

where m_e is the mass of electron, e is charge of electron, $n_s = \kappa B/(Pce)$ is the number density of the pair plasma, κ is the ratio of the number density of the pair plasma to the Goldreich–Julian number density $n_{GJ} = B/(Pce)$, $B = B_d(r/R_{NS})^3$ is the magnetic field strength, P is the period of the pulsar, and c is the speed of light. For typical pulsar parameters with period $P = 1$ second, dipolar magnetic field $B_d = 10^{12}$ gauss, and radius $R_{NS} = 10$ km, the corresponding plasma

frequency ω_p in PFR can be obtained by the Lorentz transformation to be

$$\omega_p = \frac{\omega_{p,\text{OFR}}}{\gamma_s} \approx 10^8 \left(\frac{200}{\gamma_s} \right) \sqrt{\left(\frac{\kappa}{10^4} \right) \left(\frac{1 \text{ s}}{P} \right) \left(\frac{500 \text{ km}}{r} \right)^3} \text{ rad s}^{-1}, \quad (8)$$

where the Lorentz factor γ_s was discussed in Section 1.

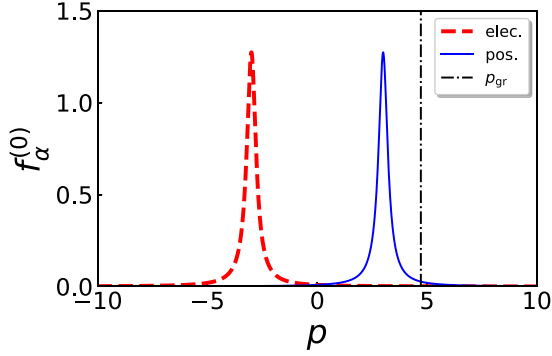
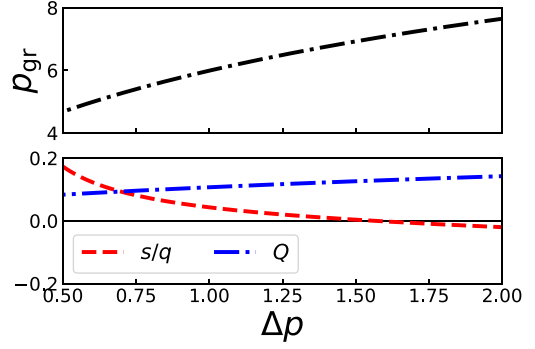
The coefficients (G_d , q_d , s_d) depend only on the plasma particles' momentum DF (see equations B7, B9, and B12 in Appendix B). Therefore, we now review various relevant models of DF so as to justify its representative forms that we will use in this study. As stated in Section 1, it is well established that normal-period radio pulsars have a strong non-dipolar surface component (see Arumugasamy & Mitra 2019 and the references therein) along with an thermionic ion flow from the surface (Cheng & Ruderman 1980; Gil et al. 2003). While some semi-analytical estimates of the pair cascade in strong non-dipolar fields have been made (Szary et al. 2015), the generic shape of the pair plasma DF is not known. However, numerical simulations like those by Arendt & Eilek (2002) show that the shape of the DF is strongly affected by the opening angle between the ambient magnetic field and the initial seed photon, the strength of the magnetic field and the seed photon energy. Namely, for low-opening angles, the DF is well described by the Jüttner–Synge distribution, so that the number of particles with high dimensionless momenta p (defined in equation 9) falls off as $\exp(-K(\ln p/p_0)^2)$, where K is inverse width of the DF and p_0 is the dimensionless momentum corresponding to the peak of the DF. In this paper, we refer to this behaviour of the DF as ‘short-tailed’. On the other hand, at large opening angles, the DF of the number of particles was found to fall off as $\exp(-p^{0.2})$ at high momenta. In general, Arendt & Eilek (2002) found these latter DFs to be significantly broader than those at small opening angles. Therefore, we refer to this type of DFs as ‘long-tailed’. It must be kept in mind that the simulations by Arendt & Eilek (2002) assume the initial seed photons to be mono-energetic, and relaxing this condition may lead to significant changes in the resulting DFs. Among other pair cascade models, like those by Hibschan & Arons (2001) and by Suvorov & Chugunov (1973) exhibit the presence of a power-law ‘long-tail’ that falls off inversely as the third power of the particle momentum. On the other hand, Monte Carlo models used by Daugherty & Harding (1982) show a ‘short-tail’ in the particle DF (see fig. 5 of Hibschan & Arons 2001 for comparison). Thus, earlier studies demonstrate the possibility of having both types, short- and long-tailed DFs in pulsar plasma.

For the soliton formation based on the NLSE model (3), we will show below that the presence/absence of an extended tail in the DF is of paramount importance. Namely, it eventually determines the number of plasma particles contributing to the NLD and CNL terms in the NLSE. In order to explore this aspect, we choose two representative forms of particle DF, viz., a Gaussian with an exponentially decaying tail (‘short-tail’) and a Lorentzian with a power-law tail (‘long-tail’).

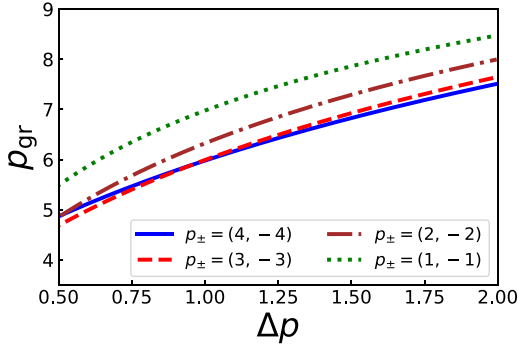
The particle DF $f_\alpha^{(0)}$ is taken to be a function of the dimensionless momentum p , which is defined as

$$p = \frac{P_\alpha}{m_\alpha c} = \frac{\gamma m_\alpha v}{m_\alpha c} = \gamma \beta \equiv \frac{\beta}{\sqrt{1 - \beta^2}}, \quad (9)$$

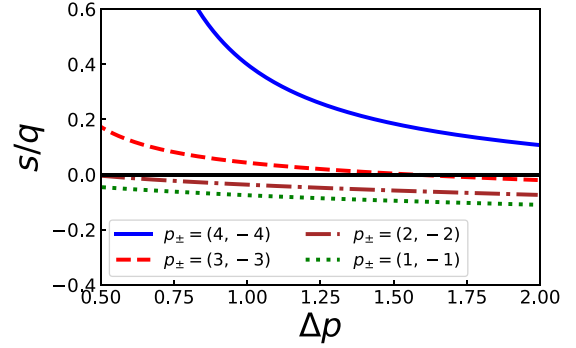
where P_α is the relativistic momentum and m_α is the mass of the plasma particles of the α th species. For the rest of the analysis, the term ‘momentum’ would be used to refer to dimensionless momentum of the plasma particles. For both Gaussian and Lorentzian


 (A) Lorentzian DF and group velocity pole with $p_{\pm} = \pm 3$ at $\Delta p = 0.5$.


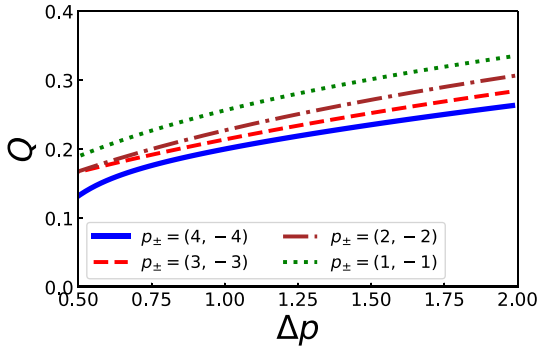
(B) Parameter space for Panel (A) as a function of temperature.



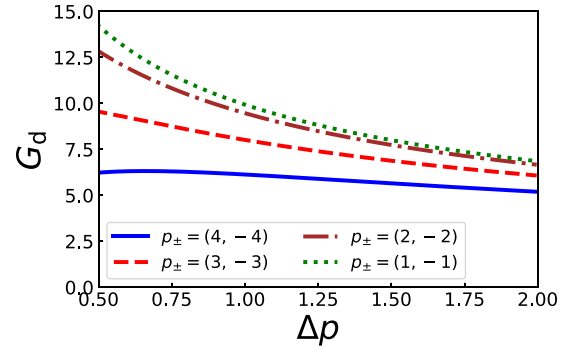
(C) The group velocity pole as a function of temperature and separation of DF.



(D) Ratio of NLD to CNL as a function of temperature and separation of DF.



(E) The Lighthill condition as a function of temperature and separation of DF.



(F) GVD as a function of temperature and separation of DF.

Figure 1. The figure shows temperature dependence of NLSE coefficients for separated Lorentzian DF as defined in equation (29). **Top:** Panel (a) shows a particular example of separated electron and positron DF along with the group velocity pole p_{gr} as defined in equation (13) for a particular temperature. Panel (b) shows the variation of p_{gr} , s/q , and q_d/G_d as a function of temperature at the same separation of DF as shown in panel (a). **Middle:** Panel (c) shows that p_{gr} at a given plasma temperature decreases as the separation of the DF increases. Panel (d) shows that the ratio s/q remains tightly clustered to values within 0.1 from zero for moderate separation of DF. Only at sufficiently high separation of DF can the s/q ratio increase to values higher than 0.5. **Lower:** Panel (e) shows that Q stays within the range (0.1, 0.3) for the range of plasma temperatures considered; in particular, the Lighthill condition (2) is satisfied. Panel (f) shows that the GVD at any temperature decreases with increasing separation.

DFs, the term ‘temperature’ will be used to refer to their widths in the momentum space. We will also sometimes refer to the tail of the Lorentzian DF as ‘high-energy’ tail, since particle energy scales approximately as momentum in the ultrarelativistic regime.

As seen from Tables B2 and B3 in Appendix B, the integrals in the dimensionless coefficients G_d , q_d , and s_d require the estimation of the group velocity of the particles. For a given DF, the wave group velocity (normalized to speed of light c) is estimated from the

expression (see equation B3 in Appendix B)

$$\beta_{gr} = \frac{1}{c} \frac{d\omega}{dk} = \frac{1 + \sum_{\alpha} \left(\frac{\omega_{p,\alpha}}{kc}\right)^2 \int_{-\infty}^{+\infty} dp \frac{\partial f_{\alpha}^{(0)}}{\partial p} \frac{\beta}{(\beta_{ph}-\beta)^2}}{\sum_{\alpha} \left(\frac{\omega_{p,\alpha}}{kc}\right)^2 \int_{-\infty}^{+\infty} dp \frac{\partial f_{\alpha}^{(0)}}{\partial p} \frac{1}{(\beta_{ph}-\beta)^2}}, \quad (10)$$

where β_{ph} corresponds to the non-dimensional phase velocity of the linear Langmuir waves (normalized to the speed of light c) and the

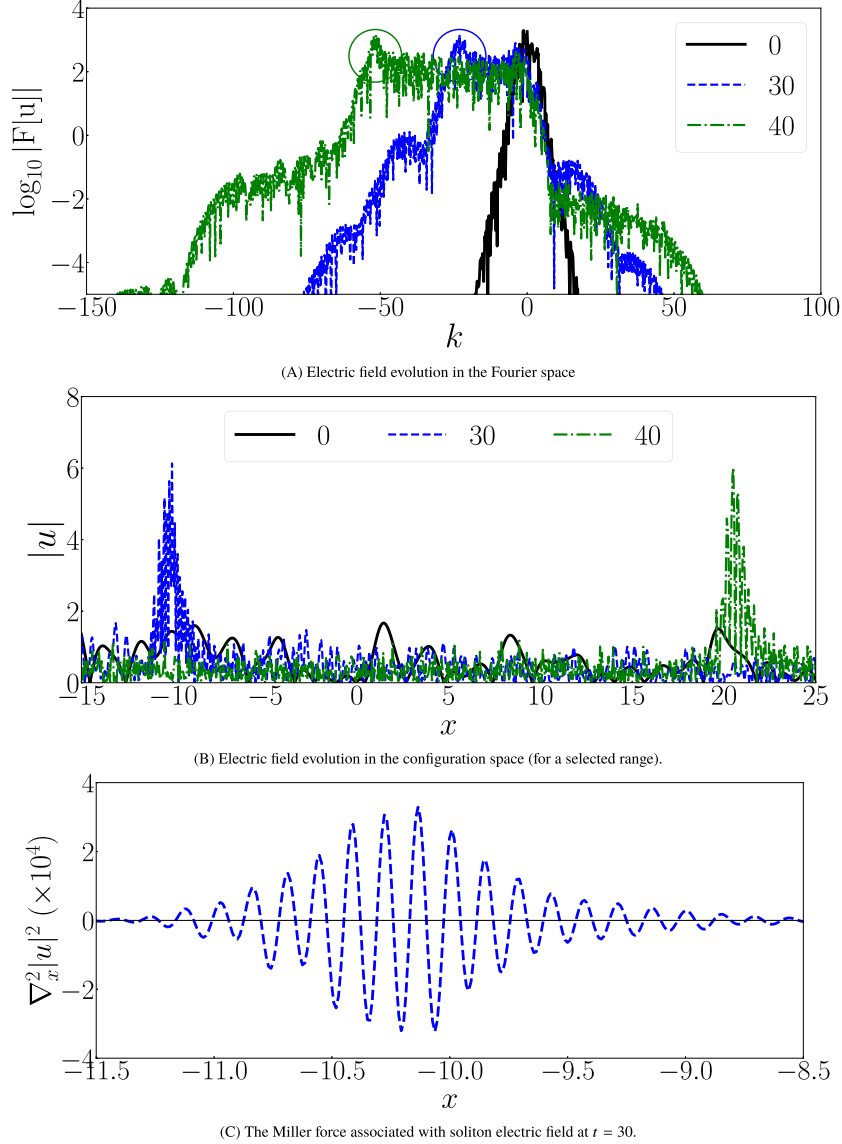


Figure 2. Simulation results of soliton formation for Lorentzian DF ($Q = 0.25$ and $s/q = 0.1$) by the numerical method described in Lakoba (2017). Panel (a) shows the movement of a prominent secondary peak (circled) to $k < 0$ at few representative times. Panel (b) shows the corresponding soliton formation in configuration space in the limited range $(-15, 25)$ for clarity. The actual simulation box has the range $(-60, 60)$. The legends in both panels indicate the dimensionless time t . The black curve in both panels shows the initial condition at $t = 0$. Panel (c) shows the Miller force associated with the soliton electric field at $t = 30$. Here, ‘soliton’ is the envelope of the pulse with $\Delta x \sim 3$ units while ripple is what appears to be a ‘carrier wave’ with wavelength $\delta x_{\text{ripple}} \sim 0.15$ units.

dimensional wavenumber k is given by the expression

$$k = \frac{1}{c} \left[\sum_{\alpha} \omega_{p,\alpha}^2 \int_{-\infty}^{+\infty} dp f_{\alpha}^{(0)} \frac{1}{\gamma^3 (\beta_{\text{ph}} - \beta)^2} \right]^{1/2}, \quad (11)$$

where $\omega_{p,\alpha}$ is the plasma frequency associated with α th species in the plasma and is defined as

$$\omega_{p,\alpha} = \sqrt{\frac{4\pi n_{\alpha} e_{\alpha}^2}{m_{\alpha}}}. \quad (12)$$

Note that the dependence of $\omega_{p,\alpha}$ on the particle species comes from its dependence on mass m_{α} , number density n_{α} , and the charge e_{α} of the species.

In Section 3, we will also extensively refer to the momentum corresponding to the group velocity, given according to equation (9),

by

$$p_{\text{gr}} = \gamma_{\text{gr}} \beta_{\text{gr}}. \quad (13)$$

This p_{gr} appears as a pole in the integrals for s_d and q_d (see Tables B2 and B3 in Appendix B). The location of this pole determines the magnitude of s/q (see equation B23 in Appendix B). Physically, $|s/q|$ is higher if the pole p_{gr} is near the peak of the DF since then the number of particles interacting with Langmuir waves is greater, and vice versa.

In Section 2.2, we discuss under what condition charge separation occurs in the configuration space and how the presence of an iron species component may potentially enhance the charge separation.

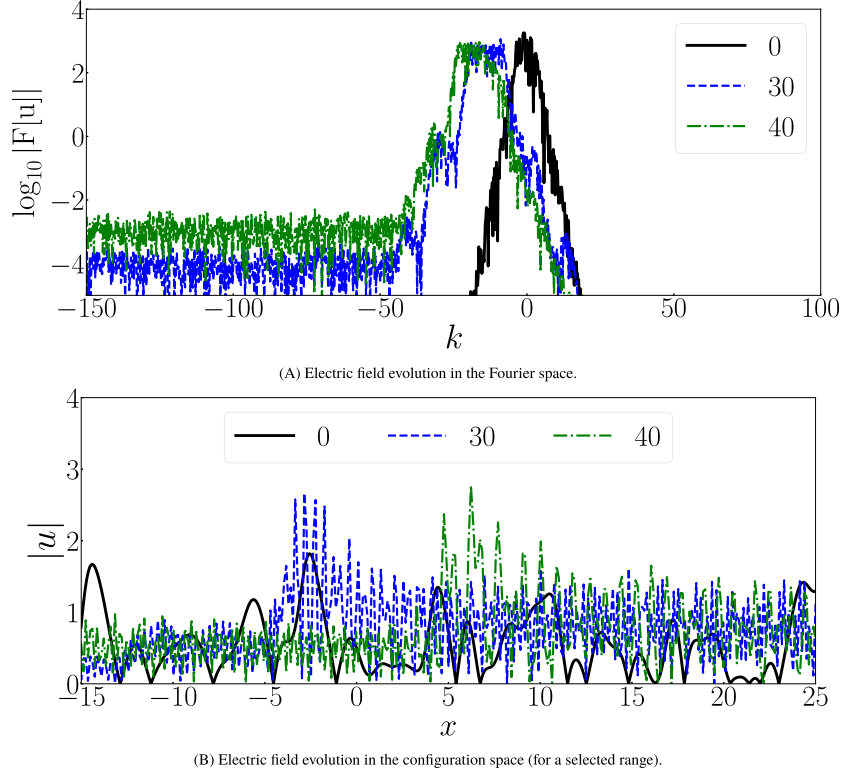


Figure 3. Simulation of pulse evolution for Lorentzian DF ($Q = 0.25$ and $s/q = 0.5$) by the numerical method described in Lakoba (2017). The black curve in both panels shows the initial condition at $t = 0$. Panel (a) shows the absence of a prominent secondary peak as was seen in Fig. 2. Panel (b) shows the corresponding wave field evolution in the configuration space in the limited range $(-15, 25)$ for clarity. The actual spatial range of the simulation box is $(-60, 60)$. It can be seen that the amplitude of the envelope of the pulses at any time does not exceed the amplitude of the initial wave electric field. Thus, soliton formation is suppressed for $s/q \gtrsim 0.5$.

2.2 Charge separation in configuration space

The slowly varying charge density (in electrostatic units per cubic centimetres) corresponding to the envelope field of equation (3) is given by (see equation A23 of MGP00)

$$\rho = \mu \left(\frac{1}{4\pi k^2 c^2} \right) \left(\frac{|e|}{m_e c^2} \right) \frac{\partial^2 |E|^2}{\partial \xi'^2}, \quad (14)$$

where

$$\mu = \frac{\sum_{\alpha} \text{sgn}(\alpha) \varphi_{\alpha} \omega_{p,\alpha}^2 \mathcal{P} \int_{-\infty}^{+\infty} dp \frac{1}{(\beta - \beta_{gr})} \frac{\partial}{\partial p} \left[\frac{(\beta - \beta_{gr})}{(\beta_{ph} - \beta)^2} \frac{\partial f_{\alpha}^{(0)}}{\partial p} \right]}{\sum_{\alpha} \omega_{p,\alpha}^2 \mathcal{P} \int_{-\infty}^{+\infty} p \frac{1}{(\beta - \beta_{gr})} \frac{\partial f_{\alpha}^{(0)}}{\partial p}}, \quad (15)$$

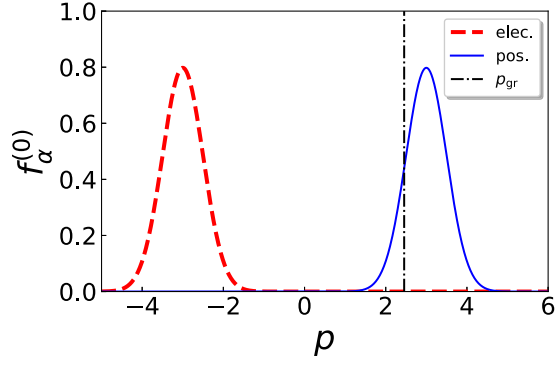
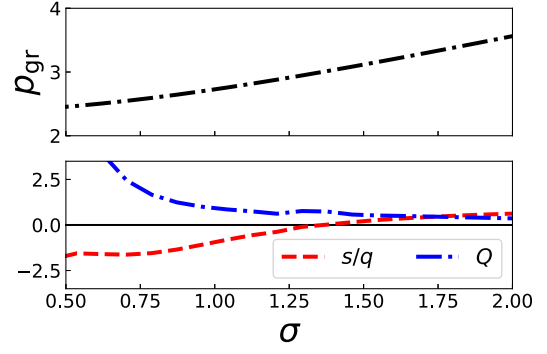
where $\text{sgn}(\alpha)$ is $+$ for positrons and ions, and is $-$ for electrons, and $\varphi_{\alpha} = (|e_{\alpha}|/e) \times (m_e/m_{\alpha})$.

Equation (15) shows that for coinciding electron and positron DF, the terms pertaining to electrons and positrons in the numerator of (14) cancel each other. Then, integral μ vanishes and there is no charge separation. Physically, this effect of charge separation can be understood as follows. The term $\partial^2 |E|^2 / \partial \xi'^2$ represents the ponderomotive/Miller force. The Miller force is a pressure force that pushes plasma particles from regions of strong to low electric fields. The force is independent of the sign of the charge particles but depends on the magnitude of charge to mass ratio of the α th plasma species. For example, in an electron-ion plasma, the Miller force can push an electron farther away compared to an ion, and hence effective charge separation can be achieved. In the case of pair plasma, since the charge to mass ratio is same for both species, there is no such

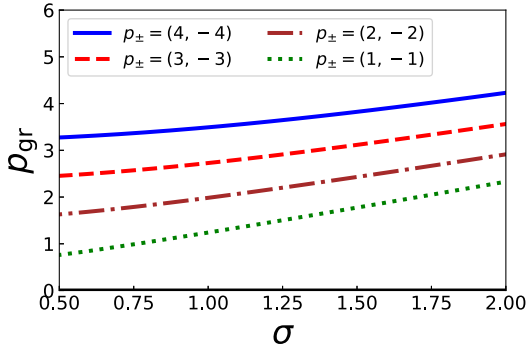
charge separation possible. Thus, in pulsar relativistic pair plasma for a coinciding electron-positron DF, no charge separation is possible. However, it was pointed out by MGP00 that due to flow of pair plasma along curved magnetic field lines, the electron and positron DF of pair plasma can separate (Cheng & Ruderman 1977; Asseo & Melikidze 1998; Paper I; also see Appendix F for full derivation) and hence relativistic masses of the electrons and positrons can be unequal. Thus, the separation of electron-positron DF can produce an effective charge separation in plasma. As shown in Paper I, the extent of the separation is determined by the arrangement of the non-dipolar surface magnetic field. For various arrangements of that field, the separation of the DF remains nearly constant for around 1000 km above the neutron star surface. In this context, we can treat the separation of the DF as a free parameter, and therefore we will consider several representative values of DF separation in Section 3.

MGP00 also suggested that the presence of an additional heavier iron ion ${}^{56}_{26}\text{Fe}$ with a high magnitude of charge component can enhance the charge separation. The PSG model provides an important motivation for inclusion of an iron ion species as an additional component in the pulsar plasma. One of the goals of this study is to find out if indeed the presence of an ion species can have appreciable effects on charge separation.

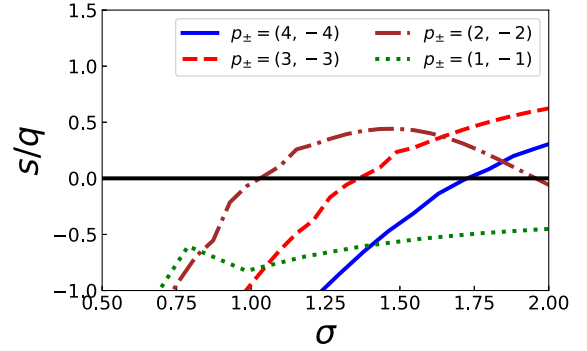
In Section 3, we will evaluate the dimensionless coefficients of NLSE expressed in equation (4) to equation (6) and the charge separation integral μ from equation (15) as a function of plasma temperature and the separation of the DF. We also include the contribution of a low-density ion component (see Appendix B3).


 (A) Gaussian DF and group velocity pole with $p_{\pm} = \pm 3$ at $\sigma = 0.5$.


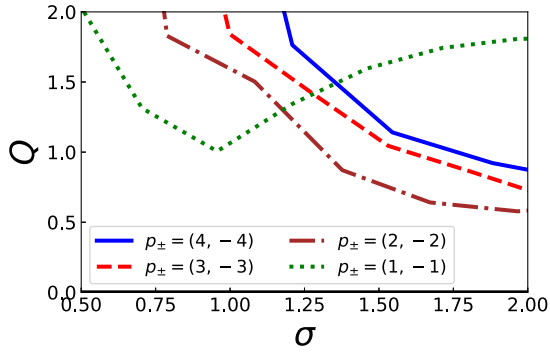
(B) Parameter space for Panel (A) as a function of temperature.



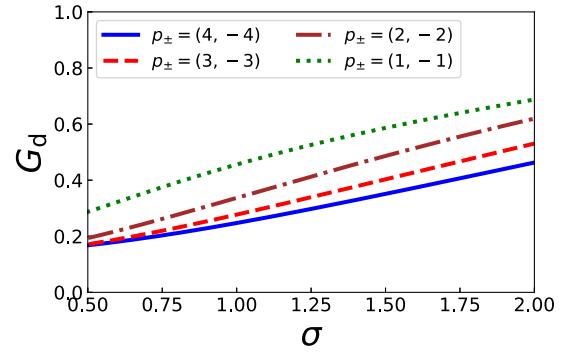
(C) The group velocity pole with temperature and DF separation.



(D) Ratio of NLD to CNL as a function of temperature and separation of DF.



(E) Lighthill condition as a function of temperature and separation of DF.



(F) GVD as a function of temperature and separation of DF.

Figure 4. The figure shows temperature dependence of NLSE coefficients for separated Gaussian DF as defined in equation (30). **Top:** Panel (a) shows a particular example of separated electron and positron DF along with the location of the group velocity at the same temperature. Panel (b) shows the variation of p_{gr} , s/q , and Q as a function of temperature at the same separation of DF as shown in panel (a). **Middle:** Panel (c) shows that the p_{gr} for a given plasma temperature increases as the separation of the DF increases. Panel (d) shows that the ratio s/q remains large for all separation of DF. The moderate values of s/q are available only near a certain temperature σ_{sp} where s/q changes sign. The value of σ_{sp} decreases with decreasing separation of the DF, until below some separation it vanishes and the magnitude of s/q ratio settles at around 0.5. **Lower:** Panel (e) shows that the Lighthill condition (2) is satisfied across the range of plasma temperatures. Panel (f) shows that the GVD remains clustered around 0.4 for all separation of DF across a wide range of plasma temperatures.

3 PARAMETER SPACE FOR NLSE FOR SOLITON FORMATION

The NLSE with NLD can be converted into the dimensionless form (see equation 20 of LMM18) as

$$i \frac{\partial u}{\partial t} + \frac{\partial^2 u}{\partial x^2} + Qu \left(|u|^2 + \frac{s}{\pi q} \mathcal{P} \int dx' \frac{|u(x', t)|^2}{x - x'} \right) = 0, \quad (16)$$

where

$$u = \frac{E}{E_0}, \quad (17)$$

$$x = \frac{\xi'}{\lambda_D}, \quad (18)$$

$$t = \frac{\omega_p G_d}{\theta^2} \tau', \quad (19)$$

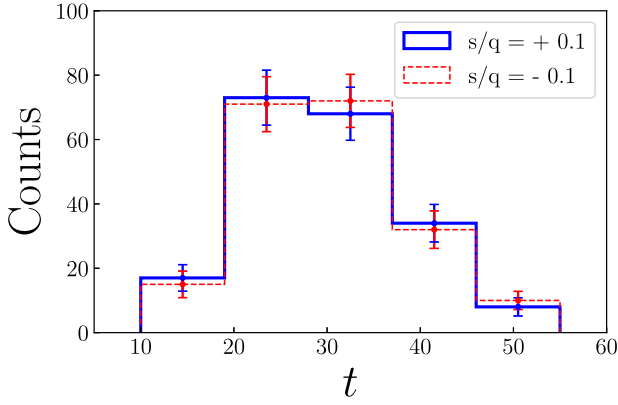


Figure 5. The figure shows the histogram for the earliest soliton formation time t (with $Q = 0.25$) that satisfies the constraint (31) for 200 random seeds in equation (25) for both positive $s/q = +0.1$ (shown in solid blue) and negative $s/q = -0.1$ (shown in dashed red). The histogram for t is divided into 5 bins in the range (10, 55) while the error bars = \sqrt{N} , where N is the number of entries in each bin. It can be seen that the average time for soliton formation is ~ 30 units for both signs of s/q .

$$Q = \left[\theta^2 \left(\frac{e}{m_e c^2} \right)^2 \left(\frac{|E_0|^2}{8\omega_p^2 \gamma} \right) \right] \left(2 \frac{q_d}{G_d} \right), \quad (20)$$

where u is the non-dimensional amplitude of the Langmuir wave envelope, x is the non-dimensional space variable, t is the non-dimensional time variable, and Q represents the non-dimensional ratio of the CNL coefficient q to the GVD. Here, the characteristic length l of the linear Langmuir waves is given by

$$l = \frac{2\pi}{k}, \quad (21)$$

where k is the wavenumber as defined in equation (11). The quantity $\theta/2\pi$ is a spatial scaling variable that characterizes the ratio of the spatial extent of the non-linear wave envelope to the characteristic length l of linear Langmuir waves. Similarly to LMM18, we will use a value $\theta = 100$ in the estimates of typical soliton properties, which will be presented in Section 3.1. For simplicity, the term in the square brackets in equation (20) for Q will be taken to equal 1, given that E_0 is an unknown field amplitude. The quantity $Q = 2q_d/G_d$ has to be positive to fulfill the Lighthill condition (2). Physically, the typical soliton formation time-scales are of the order of $\sim \mathcal{O}(1/Q)$. Thus, soliton formation is delayed for smaller Q and vice versa.

Solving equation (16) requires us to specify an initial condition. LMM18 represented the initial condition as a combination of the constant electric field component and a random electric field component. For our analysis, we discount any constant electric field and use only a completely disordered electric field (LMM18):

$$u(x, 0) = \int_{-\infty}^{+\infty} dk \frac{\hat{w}(k) \exp[-0.5(k/k_{\text{corr}})^2 - ikx]}{\sqrt{\sqrt{\pi} k_{\text{corr}}}}. \quad (22)$$

Here, k_{corr} is the wavenumber corresponding to the correlation length l_{corr} such that

$$k_{\text{corr}} = \frac{2\pi}{l_{\text{corr}}}, \quad (23)$$

and quantity $\hat{w}(k)$ denotes a white noise field described by

$$\langle \hat{w}(k_1) \hat{w}(k_2) \rangle = 0, \quad (24)$$

$$\langle \hat{w}^*(k_1) \hat{w}(k_2) \rangle = 2\delta(k_1 - k_2), \quad (25)$$

where the angle brackets denote ensemble average. Let us mention that increasing k_{corr} has the same effect as decreasing Q : they both increase the time at which solitons emerge (see table 2 of LMM18).

To solve equation (16) numerically, we use the integrating factor-leap-frog method by Lakoba (2017). Simulation parameters of the numerical scheme are summarized in Appendix C.

Next, the maximum dimensionless time for soliton formation can be estimated as follows. The derivation of equation (16) assumes that background plasma conditions as captured by the coefficients (4)–(6) are steady during the evolution of the wave electric field. For any given separation of the DF, this condition requires that the plasma frequency ω_p should not change drastically during the evolution of the wave electric field. From equation (8), the change in plasma frequency $\Delta\omega_p$ for segments of Δr km along a field line can be estimated to be $\Delta\omega_p/\omega_p = 1.5\Delta r/r$. Thus, if we choose $\Delta r = 3$ km and $r = 500$ km, the change in plasma frequency is less than 1 per cent and can indeed be neglected. Since the outflow is ultrarelativistic, a typical time-scale associated with this spatial length segment is $\Delta t_{\text{OFR}} = 3 \text{ km}/c \approx 10^{-5}$ s. We assume that the PFR moves with a Lorentz factor $\gamma_s \approx 200$ with respect to OFR. Then, the typical time-scale in the PFR is $\Delta t_{\text{PFR}} = \gamma_s \Delta t_{\text{OFR}} \approx 2 \times 10^{-3}$ s. The MFR moves relative to OFR in the same direction as PFR (away from the pulsar along the magnetic field lines) with a typical Lorentz factor $\gamma_{\text{gr}} \approx p_{\text{gr}}$ (see equation 13) with respect to PFR. Combining Lorentz factors for ultrarelativistic co-propagation (see Appendix G), we find that the maximum time-scale in MFR is

$$\tau'_{\text{max}} \approx 2p_{\text{gr}} \Delta t_{\text{PFR}}. \quad (26)$$

Next, at a typical distance of 500 km from the surface we find, using equation (19), that the maximum dimensionless time t_{max} is given by

$$t_{\text{max}} \approx 10^4 \left(\frac{\omega_p}{10^8 \text{ rad s}^{-1}} \right) \left(\frac{100}{\theta} \right)^2 G_d \tau'_{\text{max}}, \quad (27)$$

where we have used that for the typical parameters assumed in this study, $\omega_p \sim 10^8 \text{ rad s}^{-1}$ (see equation 8). In Section 3.1, we will see that in those cases when solitons are formed, one can take $p_{\text{gr}} \approx 6$ and $G_d \lesssim 10$ as representative values. Then equation (26) yields $\tau'_{\text{max}} \approx 2 \times 10^{-2}$ s and equation (27) yields the following estimate for the maximum dimensionless time t_{max} where the (3) can be applicable:

$$t_{\text{max}} \sim 2 \times 10^3 \left(\frac{\omega_p}{10^8 \text{ rad s}^{-1}} \right) \left(\frac{100}{\theta} \right)^2 \left(\frac{G_d}{10} \right) \left(\frac{\tau'_{\text{max}}}{2 \times 10^{-2} \text{ s}} \right). \quad (28)$$

Thus, for the Lorentzian DF, the maximum dimensionless time of the simulation can be restricted to about 2000 units.

In fact, we observed solitons form over dimensionless times that are some two orders of magnitude smaller than the above estimate. This indicates that either solitons can form over distances much less than the above estimate of $\Delta r = 3$ km, or that the factor in the square brackets in (20), which we had assumed to equal 1, can in fact be much smaller (thereby allowing a larger range of values for the dimensional field intensity $|E_0|^2$, or a combination of both). In other words, a large range of values for the intensity of the initial linear field will be able to lead to soliton formation as long as the condition on $|s/q|$ stated in the next subsection is fulfilled.

3.1 Lorentzian DF

Let us use the Lorentzian DF to get representative values of the ratios s/q , q_d/G_d and the dimensionless GVD G_d . After obtaining these

representative values, we will explore soliton formation numerically following the method of Lakoba (2017) and LMM18.

The Lorentzian DF for the α th species is given by

$$f_{\alpha}^{(0)} = \frac{1}{\pi} \frac{\frac{1}{2} \Delta p}{(p - p_{\alpha})^2 + (\frac{1}{2} \Delta p)^2}, \quad (29)$$

where Δp is the width of the DF and p_{α} is the peak of the DF. Here, $\alpha = \pm$ refers to the positron and the electron DF, respectively. In this section, we refer to Δp of equation (29), which characterizes the spread of particles' momenta, as 'temperature'. In relativistic hot plasma, this spread of the momenta is assumed to be a significant fraction of the mean momentum. Contrarily, in a cold plasma, the spread is small. Next, in this study we assume the peak momentum of the particle DF to vary in the range 1–3. Thus, to keep the ratio of the width to the peak in the DF to vary from the cold limit to hot limit at all values of peak separation, $p_+ - p_-$, the plasma temperature Δp is chosen to be in the range (0.5, 2.0) in this study. In dimensional units, this temperature range corresponds to 5×10^9 K to 2×10^{10} K.

We evaluate the NLSE coefficients at different separations of the DF as a function of the plasma temperature using equations B6, B9, and B12 of Appendix B. The results are shown in Fig. 1 and can be understood physically as follows. Panel (a) shows for a given separation of the DFs, the pole due to group velocity p_{gr} is at the tail of DF. The upper subpanel of panel (b) shows that the pole p_{gr} shifts to higher values as the temperature of the plasma is increased. Thus, the number of interacting particles at the group velocity decreases as the temperature is increased. It is reflected in the lower subpanel of panel (b), which shows that the magnitude of s/q decreases with increasing plasma temperature. Next, we explore the location of the pole due to group velocity p_{gr} for different separation of DF. Panel (c) shows that at a given plasma temperature (say $\Delta p = 1.0$), the pole p_{gr} shifts to lower values as the separation of the DFs increases. It means that with increasing separation of DF, the pole shifts towards the centre of the DF, thereby increasing the number of plasma particles interacting with the Langmuir waves, thereby increasing the effect of the NLD relative to the instantaneous CNL. Consequently, panel (d) shows that for moderate separation values, the magnitude of s/q is clustered within ~ 0.1 from zero for a range of plasma temperatures. However, for larger separation of DF, the magnitude of s/q increases to about 0.5 or even higher, especially for colder plasma. Finally, panel (e) shows that the quantity Q is of the order of ~ 0.25 for all separations of the DF across the range of plasma temperatures. Thus, we take $s/q = 0.1$ and 0.5 for small/moderate and for larger DF separation, respectively. The value of Q can be taken to have a constant value of 0.25.

Simulation results for ($Q = 0.25$, $s/q = 0.1$) and the initial condition (22) are shown in Fig. 2. Following LMM18, we used a representative value $k_{\text{corr}} = 2$. In panel (a), soliton formation can be clearly identified with the movement of a well-formed secondary spectral peak from $k = 0$ to $k < 0$. This peak in the Fourier spectrum corresponds to a soliton in physical space (LMM18), seen in panel (b). Panel (c) shows the Miller force associated with the envelope soliton.

The following remark about identifying soliton formation from the field's spectrum needs to be made. In panel (a), one sees that the amplitudes of the secondary peak, corresponding to the soliton in the physical space, and of the spectrum of the initial field are about the same. Yet, the amplitude of the soliton in the physical space (panel b) is several times greater than that of the initial field. Thus, this amplitude increase must occur via increased coherence of the field 'inside' the secondary spectral peak compared to the

initial fully random field. As was noted in LMM18, this formation of high-amplitude solitons out of an initial disordered state is a generic feature that occurs in many (but not all) so-called near-integrable but not exactly integrable non-linear wave models. (Here, the case $s/q = 0$ is that of the integrable NLSE with purely local cubic non-linear term; for it, formation of a long-living soliton out of a disordered state will *not* occur.) The specific contributions of this study, and earlier of LMM18, was to show that this soliton formation does indeed occur for the NLSE with a sufficiently small NLD term, *and* that it occurs within the time t_{max} that corresponds to realistic parameters in pulsar plasma. (In contrast, soliton formation in another model, considered in Jordan & Josserand 2001, occurred over a time of many tens of thousands dimensionless units.)

The simulation results for ($Q = 0.25$, $s/q = 0.5$) are shown in Fig. 3. Unlike in Fig. 2, here no spectral peak is seen to form in panel (a), and, instead, energy gets more uniformly distributed among spectral components of the field. One can interpret this as the field becoming less coherent for those larger values of s/q . In physical space (panel b), this is manifested by the absence of well-localized, long-living, and high-amplitude bunches of electric field. It must be noted that the behaviours, shown in Figs 2 and 3, at small and large s/q were found in LMM18, whereas here we demonstrated that they can actually occur in pulsar plasma.

Next, since our assumptions at the beginning of this section about the strength of the electric field (i.e. parameter Q) and the measure of disorder of the initial field (i.e. k_{corr} in 22) are somewhat arbitrary, below we explore the effect of these parameters on soliton formation. The simulation setup and technical details of the results are described in Appendix D; here, we present only their gist. First, we found that the effect of decreasing k_{corr} from 2 to 1 led only to the decrease of the soliton formation time, in accordance with the statement at the beginning of this section; no statistically significant changes were found in the distribution of the amplitude of the long-living solitons that formed. Second, we doubled the initial amplitude of $u(x, 0)$, which is tantamount to quadrupling Q . In this case, the final amplitude of the formed solitons was, on average, lower than for the original $u(x, 0)$; however, qualitatively, the distribution of the final soliton amplitudes remained similar to the original case. (We also found that, in agreement to the statement at the beginning of this section, the soliton formation time decreased approximately four-fold.)

To summarize, soliton formation for long-tailed DF can occur for a wide range of plasma temperature for moderate separations of the electron–positron DF. Large separation of the DF increases the value of s/q , which necessarily leads to suppression of soliton formation via the mechanism explained in our discussion about Fig. 1

3.2 Gaussian DF

The Gaussian DF for α th species is given by

$$f_{\alpha}^{(0)} = \frac{1}{\sqrt{2\pi}\sigma} \exp \left\{ -\frac{(p - p_{\alpha})^2}{2\sigma^2} \right\}, \quad (30)$$

where σ is the width of the DF and p_{α} is the peak of the DF. In this section, we will refer to σ as the plasma 'temperature'. Like in the previous subsection, in our study the plasma temperature σ is restricted to the range (0.5, 2.0).

Similar to the previous section, we evaluate the NLSE coefficients for different separations of the Gaussian DF as a function of the plasma temperature σ . The results are shown in Fig. 4 and can be understood physically as follows. Panel (a) shows that for a given separation of the DF, the pole due to group velocity p_{gr} is near the

centre of the positron DF. The upper subpanel of panel (b) shows that while pole p_{gr} shifts to higher values with increasing temperature, it still lies very close to the peak of the positron DF. Thus, the number of particles that can interact at the group velocity of linear Langmuir waves remains high. This is reflected in the lower subpanel of panel (b), which shows that the magnitude of s/q generally remains high across a range of σ . Next, we explore the location of p_{gr} for different separations of DF. Panel (c) shows that for all temperature values considered, the pole p_{gr} remains close to the centre of the positron DF. Panel (d) shows that small values of s/q can be obtained only in a very narrow range of σ where the quantity s/q changes sign. The location of this temperature range varies with the DF separation and, in fact, for sufficiently small separation, there is no temperature (in the range considered here) where s/q would be as small as 0.1. Namely, for $p_{\pm} \sim \pm 1$, one has $s/q \sim -0.5$.

As shown in Fig. 3 and in LMM18, higher values of $s/q \gtrsim 0.5$, observed for most temperature values in the above range, lead to suppression of soliton formation.

To summarize, the Gaussian DF provides small values of $s/q \lesssim 0.1$ only in a narrow interval of temperatures and for moderate separation of DF. As the DF separation decreases, the interval where s/q remains small, shrinks, and eventually vanishes, and the ratio stays too high: $s/q \approx -0.5$, for solitons to form. This leads us to conclude that soliton formation for short-tailed DF can occur only in a very restrictive parameter regime. As a result, short-tailed DF seems to be unlikely candidates for sustaining soliton formation under generic hot plasma conditions.

3.3 Dependence of soliton formation on sign of s/q

It can be seen from panel (d) of Figs 1 and 4 that the ratio s/q can be both positive and negative. Physically, the sign of s/q only determines the direction of the movement of the secondary peak associated with soliton formation to a higher wavenumber in the Fourier space (LMM18). For negative s/q , the secondary peak in the Fourier space moves to $k > 0$ and vice versa. Physically, there is no difference as the presence of a secondary peak for both $k > 0$ and $k < 0$ gives rise to envelope solitons in the configuration space. The soliton formation time-scale is not affected in a statistical sense. To show that this is indeed the case, we simulate soliton formation for $Q = 0.25$ for $s/q = 0.1$ and $s/q = -0.1$ for 200 random seed values for the white noise in equation (25). Fig. 5 shows the histogram for the time t of soliton formation, defined as

$$\max|u(x, t > 0)| \geq 3 \times \max|u(x, 0)|. \quad (31)$$

It can be seen that the statistics of soliton formation times indeed does not depend on the sign of s/q .

3.4 Role of ions in modifying the coefficients of NLSE

The DF of ions are expected to be near the electron and positron DF. We treat the location of the ion DF as a free parameter wherein the maximum contribution to the NLSE coefficients due to ions can only come if the centre of ion DF is near the pole p_{gr} . The setup for maximizing the contribution to NLSE coefficients due to ions is described in Appendix B4. We find that the presence of ions modify the dimensionless coefficients of NLSE (i.e. G_{d} , q_{d} , s_{d}) by less than 10^{-8} . The result can be understood qualitatively as follows. It must be noted in the PSG model (Gil et al. 2003), the number density of ions is close to 90 per cent of the Goldreich–Julian corotational number density. As defined in Section 1, κ is the ratio of the number density of the pair plasma to the Goldreich–Julian

number density. Thus, for simplicity, the ratio of the number density of pair plasma to the number density of ions can be assumed to be κ . Then, the number density of the ions is $\sim 10^4$ times smaller than that of the pair plasma while the mass of the ions is $\sim 10^4$ times higher than that of electrons and positrons. A combination of these two effects reduces the contribution of ions to the coefficients of NLSE by the factor 10^{-8} . A more expanded discussion of these aspects will be presented in the following section. We conclude that ions make negligible contribution in modifying the coefficients of NLSE.

4 TYPICAL PROPERTIES ASSOCIATED WITH LANGMUIR SOLITONS

The typical properties of Langmuir solitons such as spatial extent, structure, and charge are crucial in determining whether these solitons can be a suitable candidate for the observed coherent radio emission in pulsars. In this section, we briefly discuss these aspects.

4.1 Typical length and ripple associated with the solitons

In this section, following LMM18, we estimate the typical size of the soliton and the ripple associated with it (in dimensional units) at a distance of $r = 500$ km above the neutron star surface. Using equations (11) and (8), the typical Langmuir length-scale l in PFR is given by

$$l = \frac{2\pi}{k} = \frac{\pi c}{\omega_{\text{p}}\sqrt{\gamma}} \approx 6 \times 10^2 \left(\frac{3}{\gamma}\right)^{1/2} \text{ cm}, \quad (32)$$

where $\gamma = \int dp \sqrt{1 + p^2} f_{\alpha}^{(0)}$ is the average Lorentz factor of the electron/positron DF of the pair plasma in PFR and depends on the temperature of the particles. For the cold plasma limit, γ equals the Lorentz factor at the peak of the electron/positron DF, whereas for hot plasma, γ can be as much as twice the Lorentz factor evaluated at DF's peak. For the rest of the analysis, we choose a representative value of γ to be 3.

From panel (c) of Fig. (2), the typical size of the soliton envelope Δ_{PFR} in PFR is given as

$$\begin{aligned} \Delta_{\text{PFR}} &= \frac{\Delta \xi'}{\gamma_{\text{gr}}} = \frac{l\theta \Delta x}{\gamma_{\text{gr}}} \\ &\approx 3 \times 10^4 \left(\frac{6}{\gamma_{\text{gr}}}\right) \left(\frac{\theta}{100}\right) \left(\frac{\Delta x}{3}\right) \left(\frac{3}{\gamma}\right)^{1/2} \text{ cm}, \end{aligned} \quad (33)$$

while the typical ripple size $\Delta_{\text{ripple, PFR}}$ from panel (c) of Fig. 2 associated with the soliton in PFR is given as

$$\begin{aligned} \Delta_{\text{ripple, PFR}} &= \frac{l\theta \delta x_{\text{ripple}}}{\gamma_{\text{gr}}} \\ &\approx 10^3 \left(\frac{6}{\gamma_{\text{gr}}}\right) \left(\frac{\theta}{200}\right) \left(\frac{\delta x_{\text{ripple}}}{0.15}\right) \left(\frac{3}{\gamma}\right)^{1/2} \text{ cm}. \end{aligned} \quad (34)$$

Then, in OFR, the typical soliton size is

$$\begin{aligned} \Delta_{\text{OFR}} &= \frac{\Delta_{\text{PFR}}}{\gamma_{\text{s}}} \\ &\approx 10^2 \left(\frac{6}{\gamma_{\text{gr}}}\right) \left(\frac{\theta}{100}\right) \left(\frac{\Delta x}{3}\right) \left(\frac{3}{\gamma}\right)^{1/2} \left(\frac{200}{\gamma_{\text{s}}}\right) \text{ cm}, \end{aligned} \quad (35)$$

while the ripple size is

$$\begin{aligned} \Delta_{\text{ripple, OFR}} &= \frac{\Delta_{\text{ripple, PFR}}}{\gamma_s} \\ &\approx 5 \left(\frac{6}{\gamma_{\text{gr}}} \right) \left(\frac{\theta}{100} \right) \left(\frac{\delta x_{\text{ripple}}}{0.15} \right) \left(\frac{3}{\gamma} \right)^{1/2} \left(\frac{200}{\gamma_s} \right) \text{ cm.} \end{aligned} \quad (36)$$

For the case considered in Section 3.1 where solitons could form (i.e. $s/q = 0.1$) and for representative parameters values considered there, the typical size for the envelope and the ripple associated with solitons are about 100 and 5 cm, respectively.

These spatial scales correspond to a frequency range from 300 MHz to 6 GHz, which spans the observed broad-band frequencies of curvature radiation. For a typical radius of curvature $r_c \approx 10^8$ cm in the radio emission zone, the characteristic frequency of curvature radiation is $\nu_c \approx 3\gamma_s^3 c / 4\pi r_c \approx 2$ GHz, which indeed falls into the above range (0.3, 6) GHz. However, the calculation of an actual radiation pattern due to CCR by an *ensemble* of such rippled structures, as can be expected in pulsar plasma, is beyond the scope of this work and will be studied elsewhere.

It must also be noted that the temperature dependence of the size of the solitons is due to the average Lorentz factor γ of the plasma particles and the Lorentz factor corresponding to the group velocity of the plasma waves γ_{gr} . As mentioned earlier, γ for a high-temperature plasma can be twice as large as the Lorentz factor associated with the peak of the electron/positron DF and enters as a square root dependence in the size estimates of equations (35) and (36). As seen from panel (c) of Figs 1 and 4, the group velocity changes only marginally within the range of temperature considered. Thus, an increase in temperature can decrease the estimates of the soliton size and ripple size by at most ~ 30 per cent.

It must also be mentioned that the number of ripples within the soliton can vary significantly. Fig. 5 shows that, for ($Q = 0.25$, $s/q = 0.1$, $k_{\text{corr}} = 2$), the time of soliton formation (see equation 31) has a significant spread and depends on the particular realization of the random initial condition (22). As a result, location (in Fourier space) of the secondary spectral peak has a wide variation. In Appendix E, we show representative cases of the location of the peak in Fourier space and the Miller force associated with the solitons. We find that while the size of the solitons is roughly the same, the number of ripples within the soliton depends on the location of the secondary peak. In particular, the number of ripples increases as the secondary peak shifts towards higher k values. The impact of the variation of the ripple size on radiation pattern will be studied in an upcoming work.

4.2 Charge separation associated with Langmuir solitons

The slowly varying charge density (14) can be rewritten using equations (17), (18), and (21) as

$$\rho = \mu \left(\frac{e}{m_e c^2} \right) \frac{|E_0|^2}{4\pi k^2 c^2} \frac{1}{l^2 \theta^2} \frac{\partial |u|^2}{\partial x^2}, \quad (37)$$

where the field amplitude $|E_0|^2$ can be expressed in the form

$$|E_0|^2 = \varkappa 8\pi \rho_{\text{GJ}} \kappa c^2 \gamma, \quad (38)$$

where ρ_{GJ} is the co-rotational Goldreich–Julian charge density in OFR, κ is the ratio of the number density of the pair plasma to the co-rotational Goldreich–Julian number density, $\gamma \approx p_+$ is the average Lorentz factor of the plasma particles in PFR, and \varkappa is the ratio of the energy density associated with the envelope field and the particle energy density in PFR.

Using the same representative values as above and a typical value $\varkappa \sim 0.1$ (from MGP00), equations (37) and (38) can be combined to give

$$\frac{\rho}{\rho_{\text{GJ}}} \approx \mu \left[\left(\frac{\varkappa}{0.1} \right) \left(\frac{\gamma}{3} \right) \left(\frac{\kappa}{10^4} \right) \left(\frac{100}{\theta} \right)^2 \left(\frac{1}{4 \times 10^4} \frac{\partial |u|^2}{\partial x^2} \right) \right], \quad (39)$$

where the quantity μ defined in equation (15) can be expressed in the form

$$\mu = \mu_{\pm} + \mu_{\text{ion}}, \quad (40)$$

where μ_{\pm} is the contribution due to separation of electron–positron DF and μ_{ion} is the contribution due to iron ion DF near the pole p_{gr} (see Appendices B3 and B4). The variation of μ with temperature is shown in Fig. 6. It can be seen that separation of electron and positron DF leads to $\mu_{\pm} \sim 10$. It can also be seen that ions play negligible role in charge separation since the highest value of $\mu_{\text{ion}} \approx 10^{-4}$. The result can be understood physically as follows. The response of α th species to the Miller force ($\nabla^2 |E|^2$) depends on the mass and density of the species. We find that the very small number density of the ions and their heavier mass lead to this response being weak. On the other hand, the separation of electron and positron DF in the pair plasma changes the effective relativistic mass (‘inertia’) of the electrons and positrons. Thus, the Miller force acts differently on both species to create a spatial charge separation. Panel (a) shows that μ_{\pm} for Gaussian DF varies with temperature, while panel (b) shows that for Lorentzian DF, μ_{\pm} remains steady across a wide range of plasma temperatures. This implies that for the same separation of the DF, the effective mass is temperature dependent for short-tailed DF and is nearly temperature independent for long-tailed DF. For ions, the nature of the DF determines the number of interacting particles at p_{gr} . For ions with large mass $m_{\text{ion}} = Am_p$, where m_p is the mass of the proton and A is the atomic weight, the choice of DF has negligible effect on the change in ions’ relativistic mass.

Let us now demonstrate that there is no physically feasible solution where contribution of ions to the charge density separation could be non-negligible (i.e. comparable to the contribution from electrons and positrons). The expression μ_{ion} can be written from equations (15) and (40) as

$$\mu_{\text{ion}} \approx 10^{-4} \left[\left(\frac{\mathcal{F}}{10^5} \right) \left(\frac{10^4}{\kappa} \right) \left(\frac{Z}{26} \right)^3 \left(\frac{56}{A} \right)^2 \right], \quad (41)$$

where \mathcal{F} is the contribution from the integrals involving DF in (15) and Z is the charge of the ions. First, we note that decreasing κ , while formally increasing μ_{ion} , will *not* lead to an increased ion’s contribution to charge separation, because the latter is proportional to $\mu\kappa$ as seen in equation (39). Secondly, considering heavier ions is not an option, either, given that $A \propto Z$ and one need to increase μ_{ion} by a factor $\sim 10^4$ to bring it to the size of μ_{\pm} . Thirdly, decreasing the width of the DF so as to boost \mathcal{F} is also not an option as cold plasma approximation is non-physical for the ion DF.

5 CONCLUSIONS

As previously shown in LMM18, soliton formation in the NLSE with NLD requires small values of the ratio of the NLD to the local CNL, $|s/q| \lesssim 0.1$, and is suppressed for higher values of $|s/q| \gtrsim 0.5$. In this work, motivated by the PSG model, we consider an admixture of electron–positron pairs and ions in the pulsar plasma and derived the NLSE for the envelope of Langmuir waves in the plasma. We found that due to the low density of ions compared to the density of the pair plasma, the ion species contribute negligibly in modifying both the

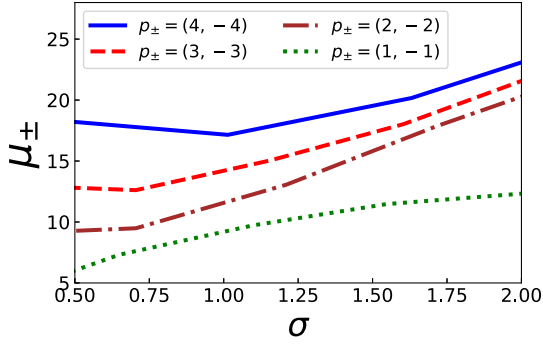
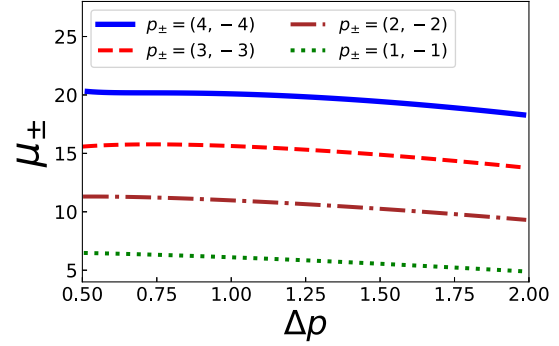
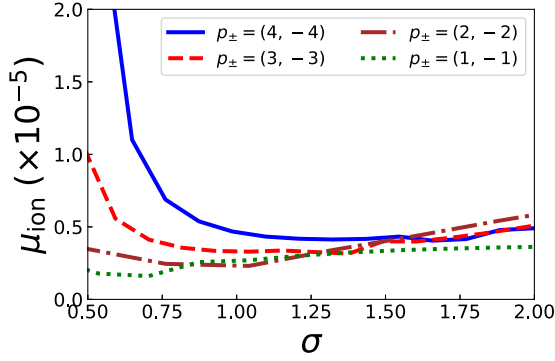
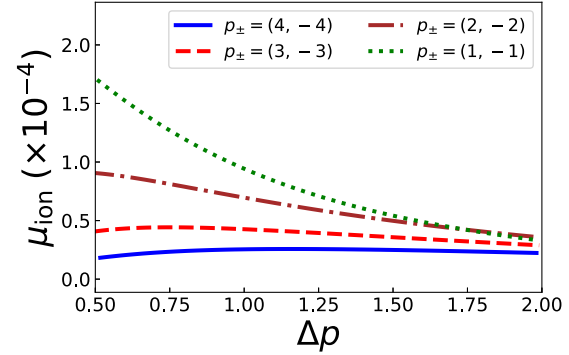
(A) Contribution to μ from separated electron-positron Gaussian DF.(B) Contribution to μ from separated electron-positron Lorentzian DF.(C) Contribution to μ for Gaussian ion DF.(D) Contribution to μ for Lorentzian ion DF.

Figure 6. Variation of the charge separation integral μ as defined in equation (15) for different separation of the DF. Panels (a) and (b) show the integral as a function of the plasma temperature for Gaussian and Lorentzian DFs, respectively. Panels (c) and (d) show the contribution to the integral due to the presence of an iron ion component. Note the vertical axis scale in panels (c) and (d) is 10^{-5} and 10^{-4} , respectively.

coefficients of the NLSE and the charge separation. For subsequent analysis, we neglected the ions and explored the parameter space of different separation of the electron and positron DF across a wide range of plasma temperatures, obtaining estimates for the range of s/q values and charge separation.

We considered two types of DF: a Lorentzian DF with a prominent power-law tail and a Gaussian DF with an exponentially decaying tail. The long-tailed Lorentzian DF provides small values of $|s/q| \sim 0.1$ across a wide range of plasma temperatures for moderate separation of the electron and positron DF. On the other hand, the short-tailed Gaussian DF provides a very restrictive parameter space where small values of $s/q \lesssim 0.1$ can be attained. In reality, the DF can have a tail in between those of a Gaussian and Lorentzian DF. However, as long as DF's tail falls off 'sufficiently slowly' for some extended range of momenta, soliton formation is feasible in pulsar plasma and thus can be considered as a viable candidate to explain occurrence of CCR charge bunches. The radiation pattern due to curvature radiation under hot plasma conditions will be treated in an upcoming work.

ACKNOWLEDGEMENTS

We thank the anonymous referee for useful comments that improved the quality of the manuscript significantly. SMR and DM acknowledge the support of the Department of Atomic Energy, Government of India, under project no. 12-R&D-TFR-5.02-0700. DM acknowledges support and funding from the 'Indo-French Centre for the Promotion

of Advanced Research – CEFIPRA' grant IFC/F5904-B/2018. This work was supported by the grant 2020/37/B/ST9/02215 of the National Science Centre, Poland.

DATA AVAILABILITY

Simulation data will be made available upon reasonable request from the corresponding author Sk. Minhajur Rahaman.

REFERENCES

- Arendt Paul N. J., Eilek J. A., 2002, *ApJ*, 581, 451
 Arumugasamy P., Mitra D., 2019, *MNRAS*, 489, 4589
 Asseo E., Melikidze G. I., 1998, *MNRAS*, 301, 59
 Basu R., Mitra D., Melikidze G. I., Maciesiak K., Skrzypczak A., Szary A., 2016, *ApJ*, 833, 29
 Blasi P., Amato E., 2011, *Astrophysics and Space Science Proceedings*, Vol. 21, High-Energy Emission from Pulsars and Their Systems: Proceedings of the First Session of the Sant Cugat Forum on Astrophysics. Springer-Verlag, Berlin, p. 624
 Cheng A. F., Ruderman M. A., 1977, *ApJ*, 212, 800
 Cheng A. F., Ruderman M. A., 1980, *ApJ*, 235, 576
 Daugherty J. K., Harding A. K., 1982, *ApJ*, 252, 337
 Geppert U., 2017, *J. Astrophys. Astron.*, 38, 46
 Gil J., Melikidze G. I., Geppert U., 2003, *A&A*, 407, 315
 Ginzburg V. L., Zheleznyakov V. V., Zaitsev V. V., 1969, *Ap&SS*, 4, 464
 Goldreich P., Julian W. H., 1969, *ApJ*, 157, 869
 Hirschman J. A., Arons J., 2001, *ApJ*, 560, 871
 Jordan R., Josserand C., 2001, *Math. Comput. Simul.*, 55, 433

- Karpman V. I., Norman C. A., Ter Haar D., Tsytovich V. N., 1975, *Phys. Scr.*, 11, 271
- Kazbegi A. Z., Machabeli G. Z., Melikidze G. I., 1991, *MNRAS*, 253, 377
- Kijak J., Gil J., 1997, *MNRAS*, 288, 631
- Kijak J., Gil J., 1998, *MNRAS*, 299, 855
- Lakoba T. I., 2017, *J. Sci. Comput.*, 72, 14
- Lakoba T., Mitra D., Melikidze G., 2018, *MNRAS*, 480, 4526 (LMM18)
- Lighthill M. J., 1967, *Proc. R. Soc. A*, 299, 28
- Lominadze D. G., Machabeli G. Z., Melikidze G. I., Pataraiia A. D., 1986, *Fiz. Plazmy*, 12, 1233
- Manthei A. C., Benáček J., Muñoz P. A., Büchner J., 2021, *A&A*, 649, A145
- Melikidze G. I., Pataraiia A. D., 1978, *Akad. Nauk Gruzii Soobshch.*, 90, 49
- Melikidze G. I., Pataraiia A. D., 1980, *Astrofizika*, 16, 161
- Melikidze G. I., Pataraya A. D., 1984, *Astrophysics*, 20, 100
- Melikidze G. I., Gil J. A., Pataraya A. D., 2000, *ApJ*, 544, 1081 (MGP00)
- Melrose D. B., 1995, *J. Astrophys. Astron.*, 16, 137
- Melrose D. B., Gedalin M. E., 1999, *ApJ*, 521, 351
- Mitra D., 2017, *J. Astrophys. Astron.*, 38, 52
- Mitra D., Li X. H., 2004, *A&A*, 421, 215
- Mitra D., Gil J., Melikidze G. I., 2009, *ApJ*, 696, L141
- Mitra D., Basu R., Melikidze G. I., Arjunwadkar M., 2020, *MNRAS*, 492, 2468
- Pataraiia A., Melikidze G., 1980, *Ap&SS*, 68, 49
- Rahaman S. M., Mitra D., Melikidze G. I., 2020, *MNRAS*, 497, 3953 (Paper I)
- Rahaman S. k. M., Basu R., Mitra D., Melikidze G. I., 2021, *MNRAS*, 500, 4139
- Ruderman M. A., Sutherland P. G., 1975, *ApJ*, 196, 51 (RS75)
- Sturrock P. A., 1971, *ApJ*, 164, 529
- Suvorov E. V., Chugunov Y. V., 1973, *Ap&SS*, 23, 189
- Szary A., Melikidze G. I., Gil J., 2015, *MNRAS*, 447, 2295

SUPPORTING INFORMATION

Supplementary data are available at [MNRAS](#) online.

Online_soliton.pdf

Figure S1. A schematic of the particle distribution function and the pole of the group velocity (shown as horizontal dashed line).

Figure S2. The histograms for cases (I)–(III) (see Appendix D) for details.

Figure S3. The figure shows the Fourier space and the configuration space for fixed ($Q = 0.25$, $s/q = 0.1$, $k_{\text{coor}} = 2$) for three different random seed values at times (shown in legends in the left-hand panel) when the amplitude of the solitons exceeds the initial field amplitude by at least three times.

Table S1. Transformation of quantities from PFR to MFR

Table S2. For α th species in the plasma, φ_α is the ratio of charge to mass in units of e/m_e and χ_α is the ratio of number density of the plasma to the number density of pair plasma.

Table S3. Classification of integrals for the coefficients in NLSE.

Table S4. Conversion of the integrals from dimensional form to dimensionless form.

Table S5. Parameters of the box used for simulation.

Please note: Oxford University Press is not responsible for the content or functionality of any supporting materials supplied by the authors. Any queries (other than missing material) should be directed to the corresponding author for the article.

This paper has been typeset from a $\text{\TeX}/\text{\LaTeX}$ file prepared by the author.

List of astronomical key words (Updated on 2020 January)

This list is common to *Monthly Notices of the Royal Astronomical Society*, *Astronomy and Astrophysics*, and *The Astrophysical Journal*. In order to ease the search, the key words are subdivided into broad categories. No more than *six* subcategories altogether should be listed for a paper.

The subcategories in boldface containing the word ‘individual’ are intended for use with specific astronomical objects; these should never be used alone, but always in combination with the most common names for the astronomical objects in question. Note that each object counts as one subcategory within the allowed limit of six.

The parts of the key words in italics are for reference only and should be omitted when the keywords are entered on the manuscript.

General

editorials, notices
errata, addenda
extraterrestrial intelligence
history and philosophy of astronomy
miscellaneous
obituaries, biographies
publications, bibliography
sociology of astronomy
standards

Physical data and processes

acceleration of particles
accretion, accretion discs
asteroseismology
astrobiology
astrochemistry
astroparticle physics
atomic data
atomic processes
black hole physics
chaos
conduction
convection
dense matter
diffusion
dynamo
elementary particles
equation of state
gravitation
gravitational lensing: micro
gravitational lensing: strong
gravitational lensing: weak
gravitational waves
hydrodynamics
instabilities
line: formation
line: identification
line: profiles
magnetic fields
magnetic reconnection
(*magnetohydrodynamics*) MHD
masers
molecular data
molecular processes
neutrinos
nuclear reactions, nucleosynthesis, abundances
opacity
plasmas
polarization

radiation: dynamics
radiation mechanisms: general
radiation mechanisms: non-thermal
radiation mechanisms: thermal
radiative transfer
relativistic processes
scattering
shock waves
solid state: refractory
solid state: volatile
turbulence
waves

Astronomical instrumentation, methods and techniques

atmospheric effects
balloons
instrumentation: adaptive optics
instrumentation: detectors
instrumentation: high angular resolution
instrumentation: interferometers
instrumentation: miscellaneous
instrumentation: photometers
instrumentation: polarimeters
instrumentation: spectrographs
light pollution
methods: analytical
methods: data analysis
methods: laboratory: atomic
methods: laboratory: molecular
methods: laboratory: solid state
methods: miscellaneous
methods: numerical
methods: observational
methods: statistical
site testing
space vehicles
space vehicles: instruments
techniques: high angular resolution
techniques: image processing
techniques: imaging spectroscopy
techniques: interferometric
techniques: miscellaneous
techniques: photometric
techniques: polarimetric
techniques: radar astronomy
techniques: radial velocities
techniques: spectroscopic
telescopes

Astronomical data bases

astronomical data bases: miscellaneous
atlases
catalogues
surveys
virtual observatory tools

Software

software: data analysis
software: development
software: documentation
software: public release
software: simulations

Astrometry and celestial mechanics

astrometry
celestial mechanics
eclipses
ephemerides
occultations
parallaxes
proper motions
reference systems
time

The Sun

Sun: abundances
Sun: activity
Sun: atmosphere
Sun: chromosphere
Sun: corona
Sun: coronal mass ejections (CMEs)
Sun: evolution
Sun: faculae, plages
Sun: filaments, prominences
Sun: flares
Sun: fundamental parameters
Sun: general
Sun: granulation
Sun: helioseismology
Sun: heliosphere
Sun: infrared
Sun: interior
Sun: magnetic fields
Sun: oscillations
Sun: particle emission
Sun: photosphere
Sun: radio radiation
Sun: rotation
(*Sun:*) solar–terrestrial relations
(*Sun:*) solar wind
(*Sun:*) sunspots
Sun: transition region
Sun: UV radiation
Sun: X-rays, gamma-rays

Planetary systems

comets: general

comets: individual: . . .

Earth
interplanetary medium
Kuiper belt: general

Kuiper belt objects: individual: . . .

meteorites, meteors, meteoroids

minor planets, asteroids: general

minor planets, asteroids: individual: . . .

Moon
Oort Cloud
planets and satellites: atmospheres
planets and satellites: aurorae
planets and satellites: composition
planets and satellites: detection
planets and satellites: dynamical evolution and stability
planets and satellites: formation
planets and satellites: fundamental parameters
planets and satellites: gaseous planets
planets and satellites: general

planets and satellites: individual: . . .

planets and satellites: interiors
planets and satellites: magnetic fields
planets and satellites: oceans
planets and satellites: physical evolution
planets and satellites: rings
planets and satellites: surfaces
planets and satellites: tectonics
planets and satellites: terrestrial planets
planet–disc interactions
planet–star interactions
protoplanetary discs
zodiacal dust

Stars

stars: abundances
stars: activity
stars: AGB and post-AGB
stars: atmospheres
(*stars:*) binaries (*including multiple*): close
(*stars:*) binaries: eclipsing
(*stars:*) binaries: general
(*stars:*) binaries: spectroscopic
(*stars:*) binaries: symbiotic
(*stars:*) binaries: visual
stars: black holes
(*stars:*) blue stragglers
(*stars:*) brown dwarfs
stars: carbon
stars: chemically peculiar
stars: chromospheres
(*stars:*) circumstellar matter
stars: coronae
stars: distances
stars: dwarf novae
stars: early-type
stars: emission-line, Be
stars: evolution
stars: flare
stars: formation
stars: fundamental parameters
(*stars:*) gamma-ray burst: general
(*stars:*) **gamma-ray burst: individual: . . .**
stars: general
(*stars:*) Hertzsprung–Russell and colour–magnitude diagrams
stars: horizontal branch
stars: imaging
stars: individual: . . .
stars: interiors

- stars: jets
- stars: kinematics and dynamics
- stars: late-type
- stars: low-mass
- stars: luminosity function, mass function
- stars: magnetars
- stars: magnetic field
- stars: massive
- stars: mass-loss
- stars: neutron
- (stars:) novae, cataclysmic variables
- stars: oscillations (*including pulsations*)
- stars: peculiar (*except chemically peculiar*)
- (stars:) planetary systems
- stars: Population II
- stars: Population III
- stars: pre-main-sequence
- stars: protostars
- (stars:) pulsars: general
- (stars:) **pulsars: individual: . . .**
- stars: rotation
- stars: solar-type
- (stars:) starspots
- stars: statistics
- (stars:) subdwarfs
- (stars:) supergiants
- (stars:) supernovae: general
- (stars:) **supernovae: individual: . . .**
- stars: variables: Cepheids
- stars: variables: Scuti
- stars: variables: general
- stars: variables: RR Lyrae
- stars: variables: S Doradus
- stars: variables: T Tauri, Herbig Ae/Be
- (stars:) white dwarfs
- stars: winds, outflows
- stars: Wolf–Rayet

Interstellar medium (ISM), nebulae

- ISM: abundances
- ISM: atoms
- ISM: bubbles
- ISM: clouds
- (ISM:) cosmic rays
- (ISM:) dust, extinction
- ISM: evolution
- ISM: general
- (ISM:) HII regions
- (ISM:) Herbig–Haro objects

ISM: individual objects: . . .

- (*except planetary nebulae*)
- ISM: jets and outflows
- ISM: kinematics and dynamics
- ISM: lines and bands
- ISM: magnetic fields
- ISM: molecules
- (ISM:) photodissociation region (PDR)
- (ISM:) planetary nebulae: general
- (ISM:) **planetary nebulae: individual: . . .**
- ISM: structure
- ISM: supernova remnants

The Galaxy

- Galaxy: abundances
- Galaxy: bulge
- Galaxy: centre
- Galaxy: disc
- Galaxy: evolution
- Galaxy: formation
- Galaxy: fundamental parameters
- Galaxy: general
- (Galaxy:) globular clusters: general
- (Galaxy:) **globular clusters: individual: . . .**
- Galaxy: halo
- Galaxy: kinematics and dynamics
- (Galaxy:) local interstellar matter
- Galaxy: nucleus
- (Galaxy:) open clusters and associations: general
- (Galaxy:) **open clusters and associations: individual: . . .**
- (Galaxy:) solar neighbourhood
- Galaxy: stellar content
- Galaxy: structure

Galaxies

- galaxies: abundances
- galaxies: active
- galaxies: bar
- (galaxies:) BL Lacertae objects: general
- (galaxies:) **BL Lacertae objects: individual: . . .**
- galaxies: bulges
- galaxies: clusters: general

galaxies: clusters: individual: . . .

- galaxies: clusters: intracluster medium
- galaxies: disc
- galaxies: distances and redshifts
- galaxies: dwarf
- galaxies: elliptical and lenticular, cD
- galaxies: evolution
- galaxies: formation
- galaxies: fundamental parameters
- galaxies: general
- galaxies: groups: general

galaxies: groups: individual: . . .

- galaxies: haloes
- galaxies: high-redshift

galaxies: individual: . . .

- galaxies: interactions
- (galaxies:) intergalactic medium
- galaxies: irregular
- galaxies: ISM
- galaxies: jets
- galaxies: kinematics and dynamics
- (galaxies:) Local Group
- galaxies: luminosity function, mass function
- (galaxies:) Magellanic Clouds
- galaxies: magnetic fields
- galaxies: nuclei
- galaxies: peculiar
- galaxies: photometry
- (galaxies:) quasars: absorption lines
- (galaxies:) quasars: emission lines
- (galaxies:) quasars: general

(galaxies:) **quasars: individual: . . .**
(galaxies:) quasars: supermassive black holes
galaxies: Seyfert
galaxies: spiral
galaxies: starburst
galaxies: star clusters: general

galaxies: star clusters: individual: . . .
galaxies: star formation
galaxies: statistics
galaxies: stellar content
galaxies: structure

Cosmology

(cosmology:) cosmic background radiation
(cosmology:) cosmological parameters
(cosmology:) dark ages, reionization, first stars
(cosmology:) dark energy
(cosmology:) dark matter
(cosmology:) diffuse radiation
(cosmology:) distance scale
(cosmology:) early Universe
(cosmology:) inflation
(cosmology:) large-scale structure of Universe
cosmology: miscellaneous
cosmology: observations
(cosmology:) primordial nucleosynthesis
cosmology: theory

Resolved and unresolved sources as a function of wavelength

gamma-rays: diffuse background
gamma-rays: galaxies
gamma-rays: galaxies: clusters
gamma-rays: general
gamma-rays: ISM
gamma-rays: stars
infrared: diffuse background
infrared: galaxies
infrared: general
infrared: ISM
infrared: planetary systems
infrared: stars
radio continuum: galaxies
radio continuum: general
radio continuum: ISM
radio continuum: planetary systems
radio continuum: stars
radio continuum: transients
radio lines: galaxies
radio lines: general
radio lines: ISM
radio lines: planetary systems
radio lines: stars
submillimetre: diffuse background
submillimetre: galaxies
submillimetre: general
submillimetre: ISM
submillimetre: planetary systems
submillimetre: stars
ultraviolet: galaxies

ultraviolet: general
ultraviolet: ISM
ultraviolet: planetary systems
ultraviolet: stars
X-rays: binaries
X-rays: bursts
X-rays: diffuse background
X-rays: galaxies
X-rays: galaxies: clusters
X-rays: general
X-rays: individual: . . .
X-rays: ISM
X-rays: stars

Transients

(transients:) black hole mergers
(transients:) black hole - neutron star mergers
(transients:) fast radio bursts
(transients:) gamma-ray bursts
(transients:) neutron star mergers
transients: novae
transients: supernovae
transients: tidal disruption events